CATALYSIS

Dry reforming of methane by stable Ni–Mo nanocatalysts on single-crystalline MgO

Youngdong Song[1], Ercan Ozdemir[2,3], Sreerangappa Ramesh[2], Aldiar Adishev[2], Saravanan Subramanian[2], Aadesh Harale[4], Mohammed Albuali[4], Bandar Abdullah Fadhel[4,5], Aqil Jamal[4,5], Dohyun Moon[6], Sun Hee Choi[6], Cafer T. Yavuz[1,2,5,7]*

Large-scale carbon fixation requires high-volume chemicals production from carbon dioxide. Dry reforming of methane could provide an economically feasible route if coke- and sintering-resistant catalysts were developed. Here, we report a molybdenum-doped nickel nanocatalyst that is stabilized at the edges of a single-crystalline magnesium oxide (MgO) support and show quantitative production of synthesis gas from dry reforming of methane. The catalyst runs more than 850 hours of continuous operation under 60 liters per unit mass of catalyst per hour reactive gas flow with no detectable coking. Synchrotron studies also show no sintering and reveal that during activation, 2.9 nanometers as synthesized crystallites move to combine into stable 17-nanometer grains at the edges of MgO crystals above the Tammann temperature. Our findings enable an industrially and economically viable path for carbon reclamation, and the "Nanocatalysts On Single Crystal Edges" technique could lead to stable catalyst designs for many challenging reactions.

Control of carbon dioxide (CO_2) emissions through avoidance, storage, and utilization has not yet been able to make an impact on excess CO_2 emissions, which already passed 40 metric gigatons per year (Gt $year^{-1}$) (*1*). The main reason is the scale: There are no feasible chemical or physical means to remove such vast quantities of CO_2. For example, human respiration alone produces more than 2.7 Gt $year^{-1}$ CO_2, and capturing that would require 27 Gt of adsorbent (at 10% w/w capacity) suited as breath catchers (*2*).

The energy demand produces the most CO_2, through fuels for mobility and electricity, and raw materials for chemical industry. Conceptually, inserting CO_2 into fuels or chemicals production without an infrastructure overhaul could provide tangible negative emissions (*3*). For example, if hydrogen production (currently 60 Mt $year^{-1}$) was from dry reforming (Eq. 1) instead of steam reforming (Eq. 2), nearly 0.5 Gt $year^{-1}$ of CO_2 would be removed immediately, matching the target set for 2030 in a decarbonization roadmap (*4*). And if vehicles used dimethyl ether (DME) as a diesel substitute, the CO_2 removal goes well above several Gt $year^{-1}$ and provides a large anthropogenic carbon sink, considering that the current CO_2 market is only 0.25 Gt $year^{-1}$ (*5*). In a "net-zero emissions energy systems" design (*6*), the endothermic reforming reactions could also store the off-peak energy in the form of synthesis gas ("syngas") or other synthetic fuels (syngas battery). Considering that a 10 Gt $year^{-1}$ CO_2 emissions cut was set by the U.S. National Academy of Sciences to occur by mid-century to enable climate recovery (*7*), dry reforming reaction becomes a promising route to tackle excess CO_2 output without disrupting current infrastructure.

$$CH_4\,(g) + CO_2\,(g) \rightarrow 2CO\,(g) + 2H_2\,(g) \quad \Delta H^{o}_{298K} = 247\ kJ\ mol^{-1} \qquad (1)$$

$$CH_4\,(g) + H_2O\,(g) \rightarrow CO\,(g) + 3H_2\,(g) \quad \Delta H^{o}_{298K} = 206\ kJ\ mol^{-1} \qquad (2)$$

$$CO\,(g) + 2H_2\,(g) \rightarrow CH_3OH\,(g) \quad \Delta H^{o}_{298K} = -91\ kJ\ mol^{-1} \qquad (3)$$

$$2CH_3OH\,(g) \rightarrow CH_3OCH_3\,(g) + H_2O\,(g) \quad \Delta H^{o}_{298K} = -24\ kJ\ mol^{-1} \qquad (4)$$

$$3CH_4\,(g) + CO_2\,(g) \rightarrow 2CH_3OCH_3\,(g) \quad \Delta H^{o}_{298K} = 250\ kJ\ mol^{-1} \qquad (5)$$

In principle, reforming reactions (Eqs. 1 and 2) can be combined to produce syngas on the scale of 20 to 30 Gt $year^{-1}$ to provide building blocks for the chemical industry, hydrogen gas for fuel cells, and fuels for power plants and existing vehicles, ultimately creating a large CO_2 emission relief. The main obstacle for this scenario, however, is the lack of durable reforming catalysts. Materials design and development is commonly suggested for such breakthroughs (*8*). The syngas would then be converted to methanol (Eq. 3) and DME (Eq. 4) through well-developed catalysts, leading to an overall reaction of natural gas with almost equal weight of CO_2 (Eq. 5) while relieving the additional water stress of steam reforming for arid countries.

Catalyst design for an industrial process always faces a "gap" between homogeneous and heterogeneous (*9*), or surface science and real-life, conditions (*10*). The difficulty arises from the lack of control on scores of active sites over the bulky catalyst surfaces because any refinement procedures attempted also change the nature of the active site composition and geometry (*11*). Dry reforming catalysts are no exception, and although nickel on magnesium oxide (Ni/MgO) was identified long ago (*12*) as a suitable non-noble catalyst, rapid coke formation and sintering have prevented its implementation at an industrial scale (*13*, *14*). Studies showed that catalyst particle size, support defects, temperature-induced aggregation, and particle composition were among the chief factors for catalyst inactivation (*15*).

In order to develop an efficient dry reforming catalyst based on Ni/MgO, we started with a highly crystalline MgO solid because we suspected that a less crystalline MgO with defects could alter the expected redox reaction between methyl anions (CH_3^-) and CO_2. Hence, we looked into near-single-crystalline MgO formation protocols. One such remarkably simple and sustainable method is the reduction of CO_2 with Mg chips through an autothermal reaction (Fig. 1 and fig. S1) (*16*). The reaction works quantitatively with nanoparticulate single-crystalline MgO forming as a smoke from a high-temperature chamber (supplementary materials). In addition to the formation of well-defined MgO cubes and cheap graphene flakes, this process also provides additional means for reclaiming CO_2.

Ni catalyst particle size is known to affect dry reforming reactions; particularly, larger sizes (such as >7 nm) were found to promote coking (*17*). Hence, we used a polyol-mediated reductive growth method in the presence of a size-limiting polyvinylpyrrolidone (PVP) polymer surfactant (Fig. 1) (*18*). Hydrazine reduction ensured no metal contamination. We found that molybdenum (Mo) addition improves catalytic conversion yields, despite the fact that Mo itself is not active for dry reforming reactions (*19*, *20*). In a typical Ni–Mo on MgO catalyst (henceforth "NiMoCat") preparation, we mixed a 10% (w/w) Ni salt and 2% Mo salt (always 5:1 ratio) to achieve 3.76% (w/w) Ni and 1.76% (w/w) Mo content in NiMoCat according to the elemental analysis performed with inductively coupled plasma mass spectrometry (ICP-MS), transmission electron microscopy–energy-dispersive x-ray (TEM-EDX), and x-ray photoelectron spectroscopy (XPS), with a molar ratio of 3.49 Ni to 1 Mo (supplementary materials).

[1]Department of Chemical and Biomolecular Engineering, Korea Advanced Institute of Science and Technology (KAIST), Daejeon, 34141 Korea. [2]Graduate School of EEWS, KAIST, Daejeon, 34141 Korea. [3]Institute of Nanotechnology, Gebze Technical University, Kocaeli, 41400 Turkey. [4]Research and Development Center, Saudi Aramco, Dhahran, 31311 Saudi Arabia. [5]Saudi-Aramco–KAIST CO_2 Management Center, KAIST, Daejeon, 34141 Korea. [6]Pohang Accelerator Laboratory, Pohang, 37673 Korea. [7]Department of Chemistry, KAIST, Daejeon, 34141 Korea.
*Corresponding author. Email: yavuz@kaist.ac.kr

As prepared, NiMoCat was tested for activity under dry reforming conditions: 50 mL min^{-1} over a 50-mg catalyst loading, 800°C, 1 bar, under a constant stream of CH_4:CO_2:He (1:1:8) (Fig. 2). After reaching sustainable conversion yields, we lowered the temperature, stepwise, to first 750°C and then 700°C. The yields went down accordingly, but we observed no deactivation. Reheating to 800°C in similar steps regained the yields. Even cooling down to room temperature under He in between temperature swings did not show any loss of catalytic activity once the conditions were reestablished.

Durability of NiMoCat was first tested under reactive conditions for up to 850 hours of continuous operation (60 L g_{cat}^{-1} $hour^{-1}$, reaction stopped because of the equipment overtime; g_{cat}, unit mass of catalyst) (Fig. 2B). After the initial heating up ("activation"), the activity was stable, and the conversions of both CH_4 and CO_2 were always near quantitative. The syngas (H_2/CO) ratio was also near unity, which is a favorable characteristic if Fisher-Tropsch was intended to follow (*14*). When these activity values are compared, NiMoCat shows far superior activity and stability over many conventional and literature catalyst examples (table S3) (*21*–*25*). We also tested NiMoCat (in pressure stable pellets) under high-pressure feeds (15 bar) with increased flow of 120 mL min^{-1} (CH_4:CO_2:N_2, 50:50:20) (Fig. 2C). The activity remained similar, proving the stability and durability of the catalyst in dry reforming of methane. In a control experiment, we increased the reactive gas flow five times to 300 L g_{cat}^{-1} $hour^{-1}$ only to record lesser conversion (80%) but no deactivation for 500 hours (Fig. 2D).

In order to understand the source of the unprecedented activity of NiMoCat, we studied spent catalysts in detail and carried out control experiments. We first checked for the degree of coking. In a thermogravimetric scan of spent catalysts, we saw increase in mass due to oxygenation but observed no combustion of carbon deposits (Fig. 2E) for all three temperatures. Electron microscopy also showed no filaments, fibers, or carbon rings around the catalysts (Fig. 1D and fig. S29). Likewise, Raman spectroscopy did not show any coking for spent NiMoCat (Fig. 2F and fig. S31). This was not true when we tested NiMoCat that was made by using commercial MgO (for example, from Sigma-Aldrich). We observed not only severe coke formation, but also the conversion yields were a lot lower, despite the same polyol synthesis for Ni–Mo nanoparticles being used (figs. S32 and S33). We also observed heavy coking when we used a different nanoparticle synthesis procedure (wet impregnation) but kept MgO the same as the active catalyst (fig. S34). The coking was predominantly around the unassociated Ni nanoparticles. Those that featured NiMoCat assembly did not show any coking (fig. S34D). Testing a commercial reforming catalyst [HiFuel (Alfa Aesar)] also yielded quick deactivation because of severe coking (fig. S35). As expected, the pristine MgO particles coked under the same conditions, pointing at active sites that could facilitate carbon deposition (figs. S3 and S4). Similarly, Ni–Mo nanoparticles without MgO support failed in only 8 hours (fig. S40).

To determine the nanoparticle size effects during catalysis, we monitored the evolution of Ni particles under synchrotron radiation (at Pohang Accelerator Laboratory) (Fig. 3) (*26*). The as-synthesized particles showed an average size of 2.88 nm but grew into 17.30 nm within 1 hour at 800°C, under reactive gas flow (activation). After prolonged activity, the particle size remained locked around 17 nm (Fig. 3). We believe that this locking mechanism is a critical factor in achieving coke- and sintering-resistant activity. We suspect that during activation, the particulates move onto the high-energy step edges of the crystalline MgO (111) and form a stable, sustained average size of 17-nm particles. An in situ TEM monitoring revealed particle movements during the temperature ramp (fig. S19 and movie S3). Although bulk Ni melts at 1455°C, it is known that Tammann temperature [minimum temperature (*T*) for solid-state mobility] for nanoparticulate Ni is 691°C (*27*). This also prevents further sintering while eliminating the risk of MgO participation in the catalytic reaction by covering the high-energy step edges. We call this phenomenon the "Nanocatalysts On Single Crystal Edges" (NOSCE) technique. A close look with high-angle annular dark-field scanning TEM (HAADF-STEM) on spent NiMoCat showed that Ni predominantly forms the NOSCE particle where Mo is spread only on Ni, without

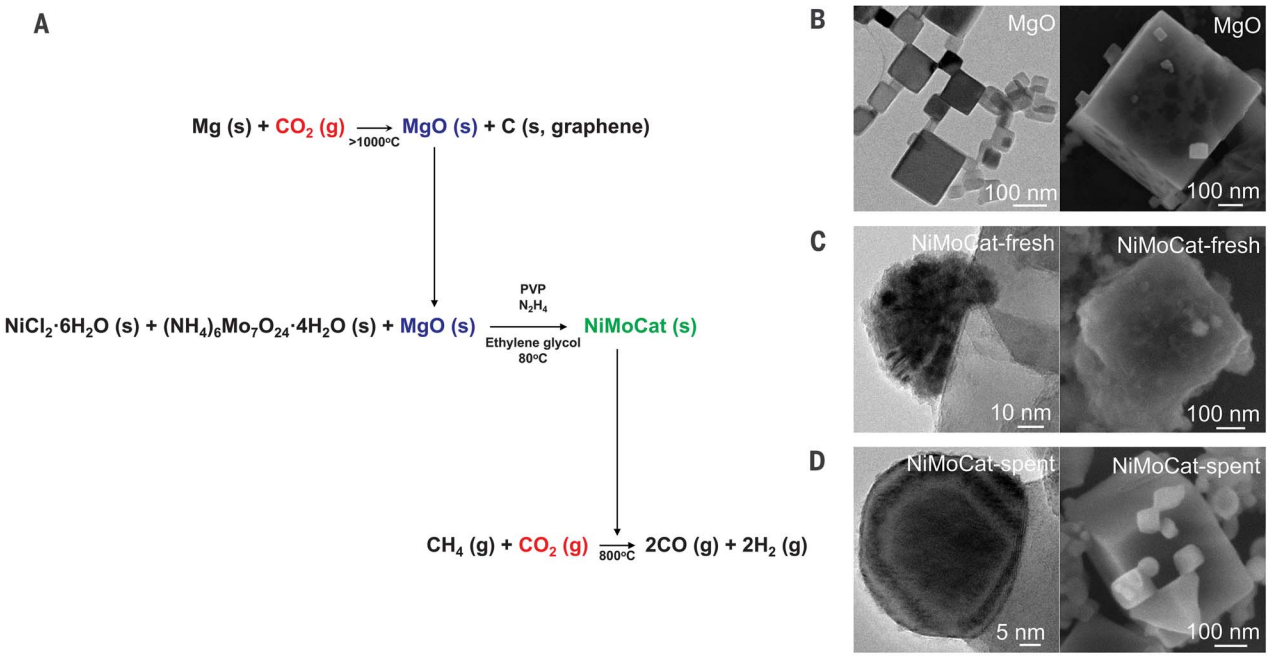

Fig. 1. Synthesis and characterization of NiMoCat. (**A**) MgO single crystals are formed from an autothermal, combustion synthesis by using Mg chips and CO_2 flow. MgO nanopowder was then dispersed into a salt solution of Ni and Mo in ethylene glycol before reduction with hydrazine. PVP ensures size control, with an average crystallite diameter of 2.9 nm. Freshly made NiMoCat was subjected to dry reforming conditions without any further treatment. (**B** to **D**) TEM (left column) and scanning electron microscopy (right column) images of (B) MgO cubes, (C) fresh NiMoCat, and (D) spent NiMoCat.

any visible interaction with the support. MgO remains as a support, with negligible leaching or spillover, as expected (Fig. 3C). Surface $Mg(OH)_2$ was also absent on the basis of the in situ Fourier transform infrared (FTIR), diffuse reflectance infrared Fourier transform spectroscopy (DRIFTS), and thermogravimetric analysis (TGA) studies (figs. S7 to S11 and S26).

In addition to the NOSCE behavior, we found that Mo doping is critical for high-conversion yields. Without Mo, the conversion is much lower (~20%), and there is an oxide layer (matching NiO d-spacings) formation (fig. S14) after 140 hours of continuous activity. If, however, higher Mo was introduced, the conversion activity was higher than without Mo but lower than the NiMoCat (~50%) (fig. S15), indicating its primary role as a promoter (fig. S16). Because Mo is only found where Ni was present (Fig. 3C), an alloy formation is likely. Mo–Ni phase diagrams (fig. S22) and bulk studies on Mo–Ni solid solutions (*28*) indicate that an atomic ratio of 3.49:1 (Ni:Mo) falls between γ- and β-MoNi (fig. S23), and the lattice spacings from high-resolution TEM (HRTEM) (Fig. 3C and fig. S24) fit very well to the predicted 73 to 78% Ni content (experimentally 77%) in a Ni-rich solid solution.

We then used x-ray absorption spectroscopy (XAS) to further understand the local structure of Mo (Fig. 4) (*29*). At 400°C, the absorption edge in x-ray absorption near-edge structure (XANES) is shifted to a higher energy because of charge transfer from Mo to nonmetal atoms but not to a level of MoO_2 or MoO_3 (fig. S25) (*30*). Two distinct peaks appear in extended x-ray absorption fine structure (EXAFS); the former at 1.3 Å (peak a) is due to Mo–C, and the latter 2.2 Å (peak b) is ascribed to scattering from neighboring Ni atoms present at the shorter distance than Mo–Mo distance. NiMoCat 400°C has substantial intensity for peak a and very weak intensity for peak b but vice versa for NiMoCat 800°C. It is explained that Mo atoms become fully dispersed on the surface of Ni–Mo particles at 400°C, and the higher temperature makes surface Mo atoms move into the interior of Ni–Mo particles for stabilization on single-crystal MgO. And the existence of Mo–C interaction (Fig. 4B) that

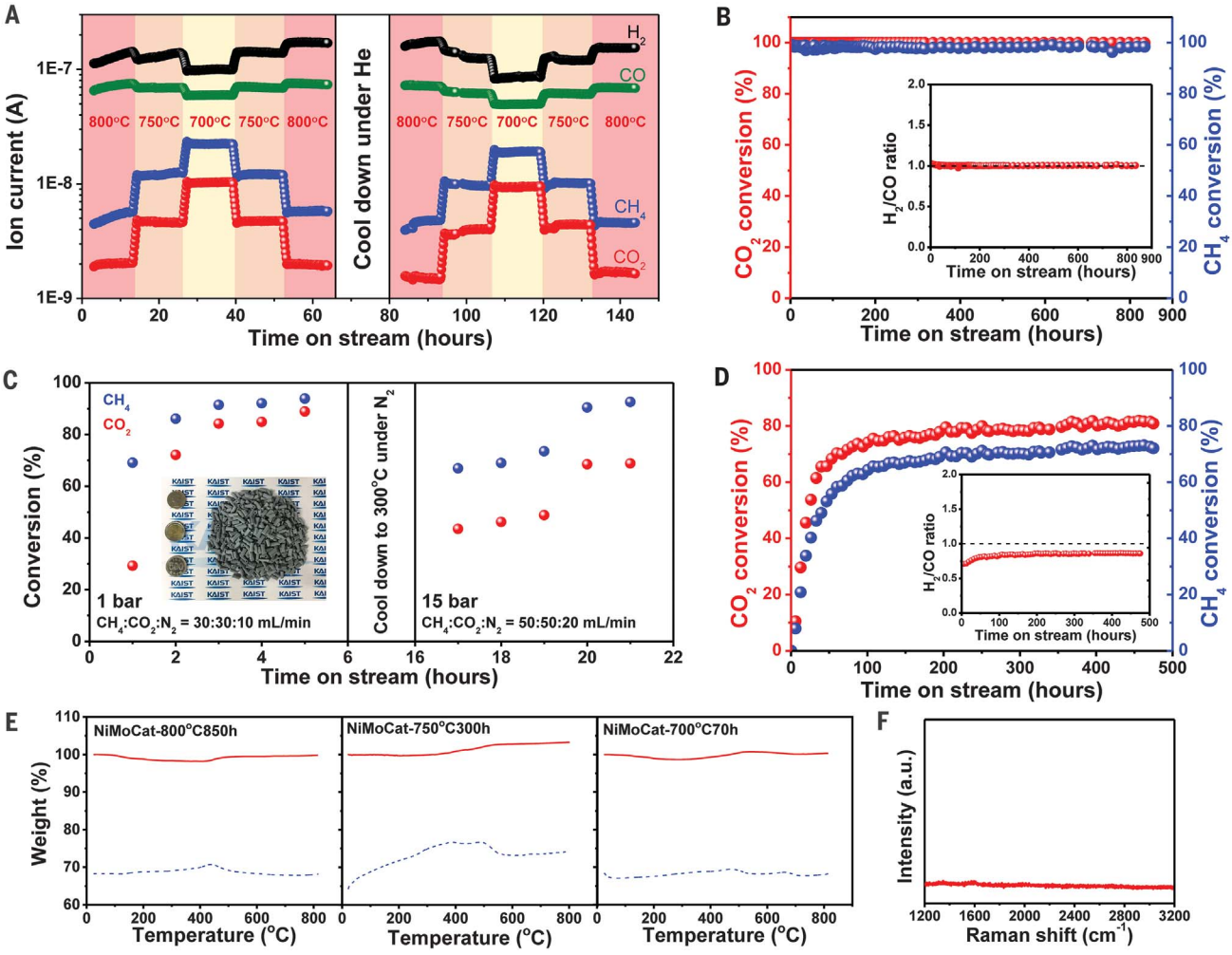

Fig. 2. Activity of NiMoCat in dry reforming of methane. (**A**) Temperature screening under reactive gas flow, 60 L g_{cat}^{-1} $hour^{-1}$. (**B**) Continuous catalytic reaction for 850 hours. (**C**) High-pressure testing for NiMoCat at 15 bar by using pellets (inset) that are formed by means of hydrocellulose binder and extrusion. (**D**) A five-times-higher gas hourly space velocity (GHSV = 300 L g_{cat}^{-1} $hour^{-1}$) run for 500 hours of continuous reaction with fresh catalyst from a new batch. No deactivation in saturation conditions (such as all active sites being in use) reflect that coke resistance is from the composition. The activation takes 0 to 5 hours, depending on the sample, hinting that as-made samples are close to the thermodynamic optimum. (**E**) TGA (solid lines, TGA; dotted lines, differential thermal analysis) of spent catalysts from varying temperature experiments, namely at 800°, 750°, and 700°C. (**F**) Raman spectra of the spent (850 hours at 800°C) NiMoCat showed no sign of coked carbon species.

gradually disappears could be another reason for the mobility of Ni–Mo nanocrystals during the NiMoCat activation.

That Ni K-edge XANES spectra in Fig. 4A reflect an electric dipole transition from 1s core level to unoccupied states of *p* type shows an increase for NiMoCat 400°C and a decrease to a level of Ni foil for NiMoCat 800°C. Correlated with the cloudy morphology owing to relaxed or broken C–C bonds in capping PVP layers at 400°C (figs. S17 to S19), such a change denotes that Ni atoms in NiMoCat become electron-deficient and then recover to the electronic state of metallic Ni with increasing temperature. On the other

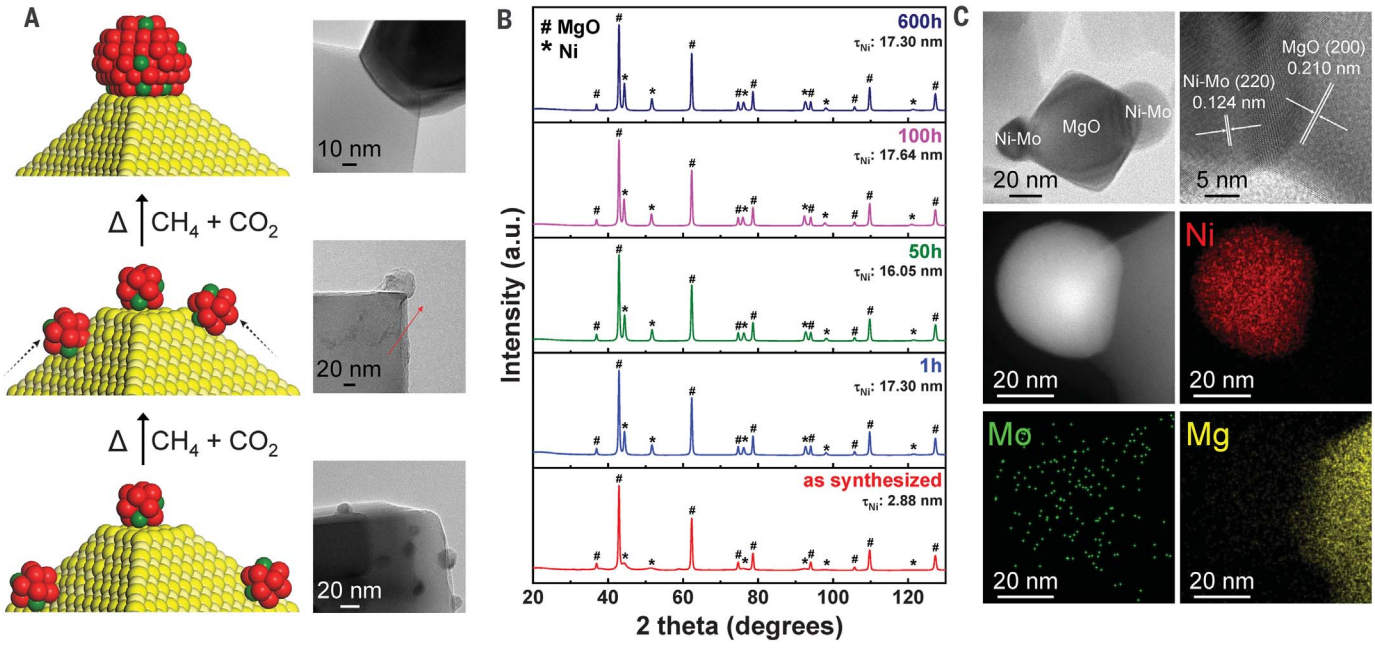

Fig. 3. NOSCE mechanism for sustained catalytic activity of NiMoCat. (**A**) Schematic for NOSCE technique. Above Tammann temperature, Mo-doped Ni crystallites move toward the edges of MgO support then unite and stabilize at the step edges. TEM images are provided as representative snapshots of each stage. (**B**) Synchrotron analysis of NiMoCat sampled at different times under reactive conditions. NiMoCat powder was packed in the 0.3-mm-diameter (wall thickness of 0.01 mm) capillary, and the diffraction data measured transparency as Debye-Scherrer at room temperature with the 63 mm of detector distance in 10 s of exposure with synchrotron radiation [wavelength (λ) = 0.90000 Å] on an ADSC Quantum-210 detector at Supramolecular Crystallography Beamline (BL2D-SMC) with a silicon (111) double-crystal monochromator (DCM) at the Pohang Accelerator Laboratory, Korea. The PAL BL2D-SMDC program (*25*) was used for data collection, and the Fit2D program was used for converted 2D to 1D pattern and wavelength and detector distance refinement. (**C**) HAADF-STEM analysis of the spent catalyst.

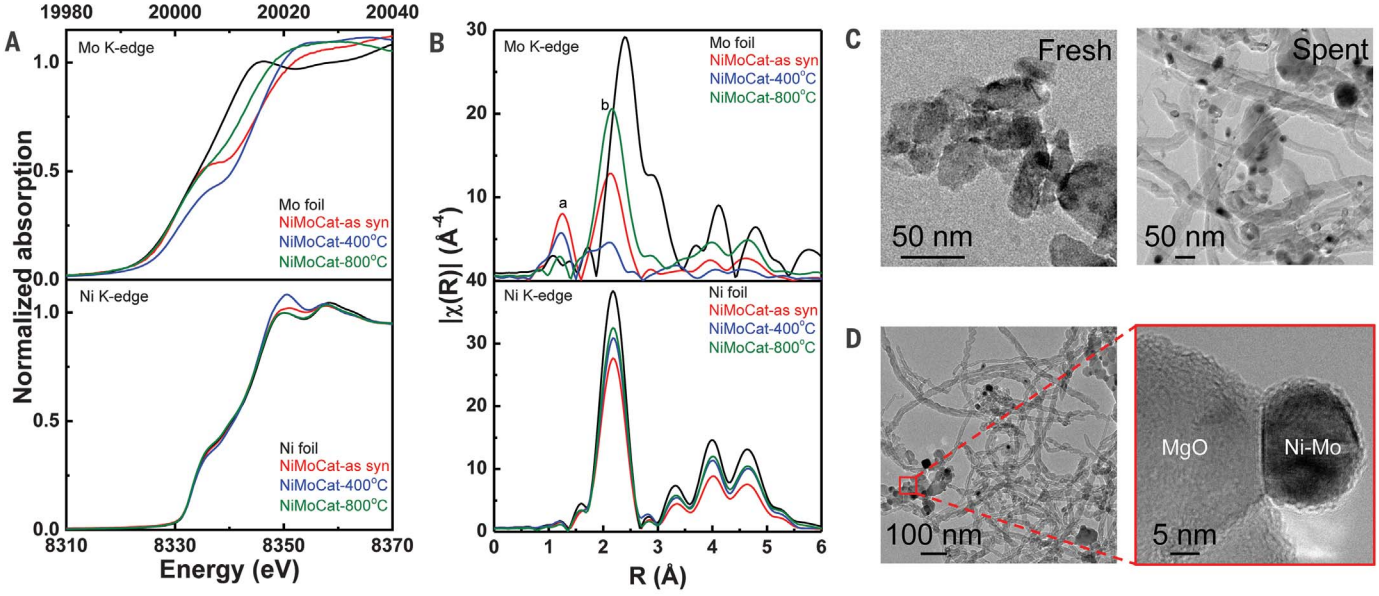

Fig. 4. Fine structure analysis and control experiments for NiMoCat. (**A**) XANES and (**B**) EXAFS of Ni K-edge and Mo K-edge during activation of NiMoCat. Bindings of Mo-C and Mo-Ni are denoted by "a" and "b," respectively. (**C**) Ball-milled activated NiMoCat before (left) and after (right) DRM reaction at identical conditions of the original catalyst. (**D**) The control catalyst that showed severe coking also contains coke-resistant assemblies that are similar to the active NiMoCat particles.

hand, EXAFS analyses in Fig. 4B explains that the particle size of Ni metallic atoms in NiMoCat are slightly increased with increasing temperature.

In order to verify the NOSCE behavior, we took fresh and activated NiMoCat and crushed it in a ball-milling apparatus (figs. S36 to S38). By doing that, we aimed to destroy the assembly of catalysts and expose new step edges by grinding the crystals, to forcefully negate the coke resistance. HRTEM showed newly appeared step edges (fig. S37). The ball-milled NiMoCat was subjected to a dry reforming experiment, and within 80 hours, we observed severe coking (Fig. 4C), whereas the parent NiMoCat ran without failing for more than 850 hours under the same reactive gas flow. Additional evidence came from the coexistence of coke-forming freestanding particles and coke-resistant NOSCE particles (Fig. 4D) because the assembly provides the correct mechanism and prevents coking by shielding step edges. Also, in a FTIR–attenuated total reflectance (ATR) study, ball-milled NiMoCat has shown enhanced CO_2 binding similar to that of the single-crystal MgO support, unlike the intact NiMoCat (fig. S39).

Last, the NOSCE particles are doing the most important work of blocking coking mechanisms but are not the only active catalysts; there are other particles (evidenced by TEM images) on the pristine MgO surfaces. Together with NOSCE, these other active sites perform exceptionally. In addition, the activity of NiMoCat was found to follow traditional DRM mechanisms (*14*) in which turn-off experiments revealed termination of activity due to oxidation (under CO_2-only feed) and severe coking (under CH_4-only feed) (figs. S43 and S44). Deliberate oxidation and reduction of the activated NiMoCat with CO_2 and H_2 revealed that the catalyst is in a dynamic equilibrium of Ni–Mo alloy and a solid solution of Ni+$NiMo_xO_y$ under DRM conditions (figs. S45 and S46).

REFERENCES AND NOTES

1. J. Tollefson, *Nature* **551**, 283 (2017).
2. H. A. Patel, J. Byun, C. T. Yavuz, *ChemSusChem* **10**, 1303–1317 (2017).
3. C. B. Field, K. J. Mach, *Science* **356**, 706–707 (2017).
4. J. Rockström *et al*., *Science* **355**, 1269–1271 (2017).
5. J. Wilcox, *Carbon Capture* (Springer-Verlag, 2012).
6. S. J. Davis *et al*., *Science* **360**, eaas9793 (2018).
7. National Academies of Sciences, and Medicine, *Negative Emissions Technologies and Reliable Sequestration: A Research Agenda* (National Academies Press, 2019).
8. *Nat. Mater.* **17**, 565 (2018).
9. A. Abad, A. Corma, H. Garcia, *Top. Catal.* **44**, 237–243 (2007).
10. C. Copéret, M. Chabanas, R. Petroff Saint-Arroman, J.-M. Basset, *Angew. Chem. Int. Ed.* **42**, 156–181 (2003).
11. J. Lu *et al*., *Science* **335**, 1205–1208 (2012).
12. F. Fisher, H. Tropsch, *Brennst. Chem.* **9**, 39–46 (1928).
13. J. M. Wei, E. Iglesia, *J. Catal.* **224**, 370–383 (2004).
14. D. Pakhare, J. Spivey, *Chem. Soc. Rev.* **43**, 7813–7837 (2014).
15. A. T. Bell, *Science* **299**, 1688–1691 (2003).
16. R. W. Dickinson, U.S. patent 8,420,042 B2, 16 April 2013.
17. J. H. Kim, D. J. Suh, T. J. Park, K. L. Kim, *Appl. Catal. A Gen.* **197**, 191–200 (2000).
18. R. Eluri, B. Paul, *J. Nanopart. Res.* **14**, 800 (2012).
19. S. M. Kim *et al*., *J. Am. Chem. Soc.* **139**, 1937–1949 (2017).
20. M. Gaillard, M. Virginie, A. Y. Khodakov, *Catal. Today* **289**, 143–150 (2017).
21. L. D. Li *et al*., *ChemCatChem* **7**, 427–433 (2015).
22. S. H. Zhang *et al*., *Catal. Today* **258**, 676–683 (2015).
23. E. Baktash, P. Littlewood, R. Schomacker, A. Thomas, P. C. Stair, *Appl. Catal. B* **179**, 122–127 (2015).
24. M. Steib, Y. Lou, A. Jentys, J. A. Lercher, *ChemCatChem* **9**, 3809–3813 (2017).
25. S. Das *et al*., *J. Catal.* **330**, 46–60 (2015).
26. J. W. Shin, K. Eom, D. Moon, *J. Synchrotron Radiat.* **23**, 369–373 (2016).
27. A. Sharma, I. Saito, H. Nakagawa, K. Miura, *Fuel* **86**, 915–920 (2007).
28. R. E. W. Casselton, W. Hume-Rothery, *J. Less Common Met.* **7**, 212–221 (1964).
29. I. I. Soykal, H. Sohn, U. S. Ozkan, *ACS Catal.* **2**, 2335–2348 (2012).
30. D. H. Youn *et al*., *ACS Nano* **8**, 5164–5173 (2014).

ACKNOWLEDGMENTS

We are grateful to W. Dickinson and M. Bishop of Dickinson Corporation for providing single-crystalline MgO nanopowder samples free of charge. We also thank J.-B. Baek of UNIST for ball-milling experiments and H. Lee of KAIST for the DRIFTS measurements. **Funding:** This work was primarily funded by the Saudi Aramco–KAIST CO_2 Management Center. C.T.Y., S.S., and A.A. also acknowledge support from National Research Foundation of Korea (NRF) grants funded by the the Korea government (MSIP) (NRF-2016R1A2B4011027 and NRF-2017M3A7B4042140). **Author contributions:** Y.S. developed NiMoCat and derivatives, tested for catalytic activity, and prepared figures. E.O. discovered NiMoCat, carried out initial activity runs, and introduced Mo for better activity. S.R. studied Mo variation, tested for activity, and scaled up NiMoCat to a total of 4 kg with help from A.A. and S.S.; A.H., M.A., B.A.F., and A.J. studied high-pressure dry reforming activities and pellet stability. D.M. measured synchrotron powder x-ray diffraction. S.H.C. carried out XAS measurements and analyzed the data. C.T.Y. conceived and supervised the project, procured funds, and wrote the manuscript, with contributions from all authors. **Competing interests:** The authors declare that Saudi Aramco–KAIST CO_2 Management Center has registered a Korean patent (KR 10-2056384) and filed provisional patent applications (AU 2017306504, DK PA201970078, CN 201780053799.2, GB 1902035.3, ES 201990013.0, IN 201947007382, SA 519401033, U.S. 16/321,028, ZA 2019/01026, SG 11201900763W, and JP 2019-528008) for the catalysts reported in this manuscript. **Data and materials availability:** All data are available in the main text or the supplementary materials.

SUPPLEMENTARY MATERIALS

science.sciencemag.org/content/367/6479/777/suppl/DC1
Materials and Methods
Figs. S1 to S46
Tables S1 to S3
References (*31*–*92*)
Movies S1 to S3

28 August 2018; resubmitted 7 October 2019
Accepted 18 December 2019
10.1126/science.aav2412

Science

Dry reforming of methane by stable Ni–Mo nanocatalysts on single-crystalline MgO

Youngdong SongErcan OzdemirSreerangappa RameshAldiar AdishevSaravanan SubramanianAadesh HaraleMohammed AlbualiBandar Abdullah FadhelAqil JamalDohyun MoonSun Hee ChoiCafer T. Yavuz

Science, 367 (6479), • DOI: 10.1126/science.aav2412

Overcoming surface defects

Dry reforming of methane with carbon dioxide creates a mixture of hydrogen and carbon monoxide—synthesis gas—which can be converted into liquid fuels. However, heterogeneous catalysts for this reaction are prone to deactivation through unwanted carbon deposition (coking) and loss of surface area of adsorbed metal nanoparticles through agglomeration (sintering). Y. Song *et al.* used highly crystalline fumed magnesium oxide to support molybdenumdoped nickel nanoparticle catalysts (see the Perspective by Chen and Xu). On heating, the nanoparticles migrated on the oxide surface to step edges to form larger, highly stable nanoparticles. This process also passivated sites for coking on the oxide to produce a catalyst with high activity and longevity at 800°C.

Science, this issue p. 777; see also p. 737

Science (ISSN 1095-9203) is published by the American Association for the Advancement of Science. 1200 New York Avenue NW, Washington, DC 20005. The title *Science* is a registered trademark of AAAS.